Chapter 5
The Key Role of Dedicated Experimental Methodologies in Revealing the Interaction Between Hydrogen and the Steel Microstructure

Tom Depover and Kim Verbeken

Abstract Understanding the interaction of hydrogen with a steel microstructure is key toward further material development and a potential future hydrogen based economy. A reliable determination of the hydrogen diffusivity and trapping are crucial hereto. Electrochemical permeation is mainly used for the former, while thermal desorption spectroscopy (TDS) is opted for the latter. Combination of both, together with a detailed microstructural evaluation, provides fundamental insights for the engineering of suitable hydrogen traps and diffusion barriers. Finally, in-situ mechanical testing enables to evaluate the hydrogen embrittlement susceptibility and identifies the active deformation mechanism. This chapter summarizes some recent experimental advances and developments of our research group. At first, focus lies on the electrochemical permeation technique, which has been expanded to apply a constant load to the materials to evaluate the influence of stresses on hydrogen diffusivity during in-situ hydrogen permeation. Elastic load on dual-phase steel increases hydrogen diffusion due to crystal lattice expansion, while plastic deformation decreases diffusion due to the formation of lattice discontinuities, e.g., dislocations. Next, the ability to assess hydrogen trapping in austenite-containing materials is critically assessed for a duplex stainless steel, revealing that the TDS data are dominated by hydrogen diffusion in these low diffusivity materials. In-situ interrupted tensile testing on these materials is further complemented with scanning electron microscopy—electron backscatter diffraction analysis. ε- and α'-martensite are found in austenite of the hydrogen-charged tensile specimens, while these martensitic transformation do not show in the uncharged samples. This is, among others, explained by a reduction in stacking fault energy due to the presence of hydrogen. Hydrogen-assisted cracks also initiate in these materials, mainly in the austenite phase. Finally, the hydrogen sensitivity is evaluated for high strength-low ductility Fe–C steels. Due to

T. Depover (✉) · K. Verbeken
Research group Sustainable Materials Science, Department of Materials, Textiles and Chemical Engineering, Ghent University (UGent), Technologiepark 46, 9052 Ghent, Belgium
e-mail: tom.depover@ugent.be

K. Verbeken
e-mail: kim.verbeken@ugent.be

V. A. Polyanskiy and A. K. Belyaev (eds.), *Advances in Hydrogen Embrittlement Study*, Advanced Structured Materials 143, https://doi.org/10.1007/978-3-030-66948-5_5

their brittle nature, a novel in-situ three-point bending setup is developed to evaluate their sensitivity to hydrogen. Hydrogen causes a transition from a microvoid (Fe–0.2C), intergranular (Fe–1.1C), or mixed (Fe–0.4C) fracture surface (air-tested samples), to a hydrogen-induced cleavage fracture appearance. This is accredited by the Hydrogen Enhanced Plasticity Mediated Decohesion mechanism, proposing that hydrogen is preferentially trapped at packet or block boundaries in high carbon steels, while lath martensitic boundaries play a minor role in the crack development.

Keywords Hydrogen embrittlement · Thermal desorption spectroscopy · In-situ mechanical testing · Electrochemical permeation · Hydrogen-assisted cracking

5.1 Introduction

The increased global warming awareness, the limited amount of fossil fuels and concerns about nuclear energy, offer challenges to scientists to provide ecological friendly solutions to deal with these climate-related concerns. As a clean energy vector, a fuel and a feedstock, clean hydrogen has the potential to accelerate the decarbonization of our energy system and of our industrial production pathways. Hydrogen is thus an attractive candidate to replace fossil fuels since its combustion only generates water avoiding the emission of greenhouse gasses. Despite these benefits, hydrogen entails a negative connotation linked to several incidents demonstrating its potential hazard [1], together with the ongoing debate and lack of understanding on the role of hydrogen on the structural mechanical integrity of metals. Besides the development of the hydrogen economy, lowering the fuel consumption of vehicles comprises another approach to make transportation more environmental friendly. Therefore, the use of high-strength steels is encouraged in the automotive industry as it may yield an increased safety together with vehicle's weight reduction, mandatory to meet the rigorous CO_2 emission regulations. Unfortunately, these steels are assumed to be prone to hydrogen-induced degradation [2–4]. Furthermore, steel alloys for the offshore industry are often protected against corrosion by impressed current cathodic protection. Though, when cathodic overprotection takes place, atomic hydrogen can absorb into material's microstructure, causing a degradation of the structural mechanical integrity [5].

Johnson [6] was the first to refer to the detrimental role of hydrogen on the mechanical performance. This pioneering work inspired many researchers, leading to several reference works in the field [7–14]. Recently, the interest in the topic got significantly reinforced by the development of numerous applications involving potential interaction with hydrogen, such as oil and gas pipelines, automotive, storage tanks, offshore structures, and welds [15–17]. The particular detrimental effect of atomic hydrogen on the material's integrity is known as the hydrogen embrittlement phenomenon or hydrogen-assisted cracking. The presence of hydrogen in a material can lead to a reduced ductility, toughness, and ultimate tensile strength, possibly triggering unpredictable failure. The four most cited mechanisms to explain hydrogen embrittlement

in non-hydride forming materials are Hydrogen Enhanced DEcohesion (HEDE) [18], Hydrogen Enhanced Localized Plasticity (HELP) [19], Adsorption Induced Dislocation Emission (AIDE) [20, 21], and Hydrogen Enhanced Strain-Induced Vacancy (HESIV) [22]. HEDE considers a decrease in cohesive bond strength between the metal atoms in the presence of hydrogen, leading to brittle crack propagation under tensile load. HELP proposes an increased dislocation mobility due to the presence of hydrogen, causing highly localized plastic deformation and finally accelerated failure [23–25]. AIDE combines HEDE and HELP, as it comprises localized plasticity, though the theory proposes that this localized plasticity takes place close to the surface at regions of stress concentrations, e.g., crack tips, including nano-voids ahead. Finally, HESIV proposes that the focus regarding the crucial factor for degradation is shifted from hydrogen to vacancies. The theory states that hydrogen promotes the formation of vacancies upon straining and thus reduces the resistance against ductile crack growth. Nevertheless, although the detrimental hydrogen effect was already discussed in [6] and several mechanisms have been proposed so far, no full comprehension of the phenomenon governing the observed ductility loss has been achieved and complex microstructures complicate our understanding. Conclusively, the potential and safe application of hydrogen still offers major challenges to the materials engineer within the frame of a clearly renewed interest in this research field.

A dedicated experimental methodology is required to gain fundamental understanding on the role of hydrogen on the structure/property relationship. Generally, the presence of hydrogen is known to deteriorate the mechanical performance of steel. However, a critical hydrogen concentration is required to initiate and propagate a crack in the metal microstructure. The susceptibility to hydrogen-induced degradation thus depends on the amount of hydrogen able to diffuse to specific, e.g., stressed, regions in the microstructure. Though, besides the hydrogen concentration, the ability to reach these critical zones is a key parameter as well. This ability is described by the hydrogen diffusion coefficient. Depover et al. [26] visualized the role of hydrogen diffusion by inspecting the fracture surfaces of in-situ charged tensile specimens, tested at different crosshead deformation speeds. The calculated hydrogen diffusion distance, i.e., penetration depth from the edges, is depending on the applied deformation speed. These distances matched perfectly well with the detected transition between hydrogen-induced brittle and ductile fracture features on the fracture surface. The prominent effect of hydrogen diffusivity was further established by in-situ hydrogen tensile testing. Generally, the ductility loss was more pronounced at lower deformation speeds [4, 27], since hydrogen had more time to diffuse and accumulate at critical regions. Hence, the critical hydrogen concentration for crack initiation was reached faster. Hydrogen can indeed accumulate at hydrostatic stress fields ahead of, e.g., a notch or crack tip. Depover et al. [28] evaluated the influence of the local hydrostatic stress state and the resulting local hydrogen concentration on the hydrogen-induced degradation. The maximal concentration of hydrostatic stress and related hydrogen concentration was located in front of the notch tip. When inspecting the fracture surface of the dual-phase steel samples, the present alumina inclusions in this material showed significant embrittlement in the region where hydrostatic stresses and hydrogen concentration peaked. More-

over, hydrogen-induced fish-eyes were found surrounding these inclusions, only at these specific regions of increased hydrostatic stress. Lastly, the synergetic effect of both hydrogen content and hydrogen diffusivity was confirmed in [27]. This work nicely demonstrated that the link between the amount of hydrogen and the hydrogen embrittlement degree is incomplete without integrating hydrogen diffusion into the discussion.

Besides the importance of hydrogen diffusion, the concept of hydrogen trapping offers significant opportunities to tweak the material design toward an improved resistance against hydrogen embrittlement. An important tool to evaluate the hydrogen trapping characteristics is thermal desorption spectroscopy (TDS). This technique is used to evaluate the distribution of hydrogen within a crystal lattice and its discontinuities [29–32]. Hence, hydrogen trapping at microstructural features and defects can be considered. Every type of trap is characterized by a particular desorption activation energy (E_a), being the energy needed for hydrogen to be released from the trapping site. Desorption activation energies can be determined by the Kissinger equation [33] by TDS measurements at different applied heating rates, as introduced by Lee and co-workers [34–36]. However, some recent literature debated the restrictions of the Kissinger equation, especially during diffusion controlled processes, as the possible delay by slow hydrogen diffusion is neglected in the referred approach [31, 37]. Lattice diffusion in body centered cubic (bcc) iron shows a low E_a (8 kJ/mol [38]), while microstructural discontinuities entail significantly higher binding energies (20–60 kJ/mol [29, 31, 32, 39–42]), while precipitates can even reach higher binding energies [30, 43–48]. Consequently, the E_a can be determined in a trustworthy way by means of the Kissinger equation, based on TDS desorption profiles at different heating rates. However, lattice diffusion in face centered cubic (fcc) iron entails a much higher E_a (51–55 kJ/mol). Since the binding energy between hydrogen and microstructural defects is similar to bcc iron, this largely impacts the capacity of TDS to characterize microstructural trapping in fcc metals [49].

Finally, in-situ mechanical testing allows the evaluation of the hydrogen embrittlement susceptibility. By interrupted in-site tensile testing, the active deformation mechanism can be identified by scanning electron microscopy—electron backscatter diffraction (SEM-EBSD) analysis. Laureys et al. [50–52] discussed this specific topic in TRIP steel where retained austenite transformed to α'-martensite upon tensile straining, creating crack initiation sites inside the martensite islands. The martensitic phase is considered to be highly susceptible to hydrogen embrittlement and thus the hydrogen-enriched martensite is very prone to hydrogen-induced cracking. Depover et al. [53] recently verified these observations during in-situ SEM micromechanical testing. Although conventional in-situ hydrogen tensile testing allows a quick and reliable screening method to evaluate the sensitivity to hydrogen embrittlement, the method is not suitable for all materials. This was demonstrated in [27], where lab cast Fe-0.2C and Fe-0.4C alloys were prepared to compare the behavior of different microstructural constituents, i.e., ferrite, pearlite, bainite, and martensite, induced by dedicated heat treatments. Conventional in-situ testing yielded trustworthy results for most of these prepared alloys. Only for the Fe-0.4C materials with a martensitic microstructure, the hydrogen-charged tensile specimens broke upon clamping in the

tensile machine. For these high strength-low ductility materials, conventional tensile testing is no longer appropriate to evaluate the proneness to hydrogen. An alternative methodology is, therefore, needed.

This work provides an overview of some of our recent work on the interaction of hydrogen with a steel microstructure. At first, the effect of constant tensile load on the hydrogen diffusivity will be characterized by electrochemical hydrogen permeation experiments during in-situ constant loading on dual-phase steel. Then, a critical assessment of the evaluation of hydrogen trapping of low hydrogen diffusion materials will be presented. For this purpose, duplex stainless steels will be characterized by TDS, combining both ferrite (bcc) and austenite (fcc) to assess the difficulties in interpreting the TDS data with respect to hydrogen trapping. Furthermore, the role of hydrogen on the active deformation mechanism in these materials will be considered as well by interrupted in-situ tensile testing combined with SEM-EBSD characterization. The initiation for hydrogen-assisted cracking will be assessed as well. Finally, the development of a novel in-situ bending technique to evaluate the hydrogen embrittlement sensitivity of brittle materials will be introduced based on lab cast Fe–C alloys, while the operational hydrogen embrittlement mechanism in these materials will be addressed based on SEM fractography.

5.2 Experimental Procedure

5.2.1 Materials Characterization

5.2.1.1 Commercial Steel Grades

The commercial steel grades considered in this work are dual-phase (DP) steel and duplex stainless steel 2205. The first considered material is the DP steel, consisting of ferrite matrix with 23.6% of martensite. The grain sizes of the ferritic and martensitic grains are about 7 μm and 2 μm, respectively. More details can be found in [26]. The thickness of the DP steel sheets was 1.1 mm, reached after hot and cold rolling, followed by subsequent annealing via industrial annealing parameters required to obtain the desired microstructure. The chemical compositions is presented in Table 5.1. The DP ferrite-martensite microstructure results in a good combination of strength and ductility, making them attractive steel grades for automotive applications. However, the mechanical contrast between both phases contains specific hazards, which are even more pronounced in the presence of hydrogen [54–56]. Therefore, this grade deserves further attention toward its hydrogen characteristics under an applied mechanical load. Inclusions were also detected in this material, identified as alumina particles by energy dispersive X-ray analysis. Unfortunately, these oxides were not homogeneously dispersed. Moreover, tensile stresses can concentrate at incoherent regions, i.e., a sharp edge or tip of the inclusion, creating a triaxial stress field where hydrogen will preferentially accumulate [57]. Therefore, a small scatter on the permeation data can be expected.

Table 5.1 Chemical compositions commercial steel grades (in wt%)

Wt%	C	Cr	fNi	Mo	fMn	Si	Other
DP steel	0.08	0.568	0.025	0.005	0.948	0.129	Cu 0.019, P 0.037, V 0.005, S 0.003, Al 0.028
UNS S32205	0.022	22.85	5.50	3.07	1.81	0.32	Cu 0.200, P 0.027, Co 0.162, N 0.173

An as-received plate of UNS S32205 duplex stainless steel with an initial thickness of 0.8 mm was studied as well. The chemical composition is included in Table 5.1. An austenite fraction of 53 ± 2% was measured by magnetic measurements (Feritscope FMP30). The grains are elongated along the rolling direction with an average thickness of 1.49±0.1 μm. More microstructural details can be found elsewhere [58, 59]. Duplex stainless steels are two-phase materials consisting of γ-austenite (fcc) and α-ferrite (bcc), showing a combination of excellent mechanical properties and corrosion resistance. The two-phase microstructure causes a complex plastic deformation behavior. Ferrite typically deforms by deformation slip due to its high amount of possible slip systems, whereas austenite can deform by different mechanisms, i.e., dislocation slip, twin formation and martensitic transformations depending, among others, on its stacking fault energy (SFE). The role of hydrogen on the active deformation mechanism in these duplex stainless steel will be evaluated by interrupted in-situ tensile testing.

5.2.1.2 Lab Cast Fe–C Alloys

Three Fe–C alloys with a different carbon content were lab cast and synthesized. The chemical composition of these generic alloys can be found in Table 5.2. The Fe–C alloys were processed by vacuum-induction melting under an argon atmosphere and hot rolled at 1100 °C till final thickness of 1.6 mm. The materials were then austenitized (50 °C > A_{c3}) for 20 min, followed by a brine water (7% NaCl) quench to obtain a fully martensitic structure. The alloys were used in their as-quenched condition to avoid the formation of cementite. More details can be found elsewhere [60]. Each alloy consisted of a martensitic structure (cf. Fig. 5.1), although Fe–1.1C had about 10 vol.% retained austenite, as revealed by X-ray diffraction [60]. Fe–1.1C also contained quench cracks, mainly propagating along the prior austenitic grain boundaries (cf. Fig. 5.1 (Fe–1.1C)). These quench cracks appear due to thermal stresses in steels having a carbon content >0.7 wt.%, since the appearance of plate martensite is necessary [61]. Moreover, when the carbon content exceeds the eutectoid composition, cementite may form along the austenitic grain boundaries during the hot rolling stage, which also facilitates cracking.

Table 5.2 Chemical compositions generic alloys (in wt%)

Wt%	C	Other (N, S, Al)
Fe–0.2C	0.222	<10 ppm
Fe–0.4C	0.421	<10 ppm
Fe–1.1C	1.111	<10 ppm

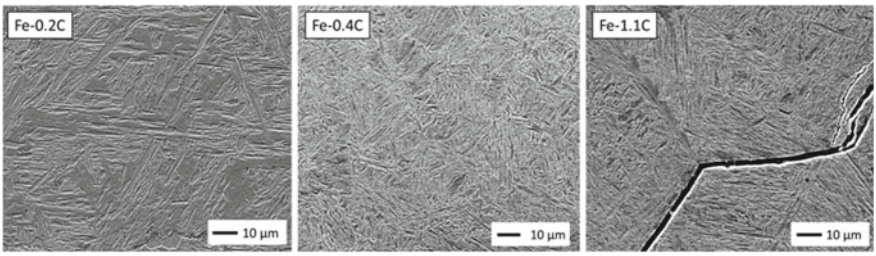

Fig. 5.1 SEM images of cross-sections of the Fe–C samples [60]. Fe–1.1C showed quench cracks. Copyright 2020, Elsevier

5.2.2 Determination of Total Hydrogen Content by Melt Extraction

Melt extraction is used to determine the hydrogen saturation level. Hydrogen was introduced in the alloys by electrochemical charging, using a 1 g/L thiourea 0.5 M H_2SO_4 solution at a current density of 0.8 mA/cm^2, for different times depending on the material of interest. The total hydrogen concentration was determined by melt extraction with an impulse furnace for heating to 1550 °C and a thermal conductivity detector for hydrogen detection. Multiple measurements were done on the duplex stainless steel and the Fe–C alloys for each applied charging time to obtain reproducible results.

5.2.3 Determination of Hydrogen Trapping Capacity Bt Thermal Desorption Spectropscopy

The hydrogen trapping sites and their activation detrapping energy were determined by performing TDS analysis for the duplex stainless steel grade. An infrared furnace to gradually heat the sample up to 950 °C and a quadrupole mass spectrometer was used for simultaneous hydrogen detection. Disc-shaped specimens were tested with a diameter of 20 mm. The thickness of this material was reduced to 0.3 mm with the same surface finish as for the melt tests. The samples were hydrogen charged, similarly as described above and two different charging times were applied, i.e.,

1 day and 15 days. Five different heating rates were applied: 900, 600, 50, 35, and 20 K/h. The method based on the work of Lee and co-workers [34–36] was used to determine the E_a of hydrogen traps related to the peaks observed in the TDS spectra. Equation (5.1) is a simplification of the original formula of Kissinger [33]:

$$\frac{\mathrm{d}\ln(\Phi/T_{\max}^2)}{d(1/T_{\max})} = \frac{E_a}{R}, \tag{5.1}$$

where Φ is the heating rate (K/min), $T_{\max}$ (K) the TDS peak temperature, E_a (J/mol) the detrapping activation energy for the specific H trap associated with $T_{\max}$ and R ($JK^{-1}mol^{-1}$) the universal gas constant. After TDS measurements using different heating rates, deconvolution of the results and determining the corresponding peak temperatures for a trap, plotting $\ln(\Phi/T_{\max}^2)$) versus $(1/T_{\max})$ allows to obtain the E_a corresponding to that specific trap.

The experimental TDS spectra of this duplex steel was complemented with a numeric diffusion model, for which both a homogeneous and heterogeneous microstructural model was developed to simulate the experimental desorption spectra [62]. Hydrogen diffusion according to Fick's law was implemented for this purpose; however, trapping was not included to verify the contribution of the latter to the experimental TDS profile. The first model assumed that the material was homogeneous with one over-all, temperature-dependant, hydrogen diffusion coefficient and an average hydrogen solubility. The second model considered the heterogeneous microstructure of the duplex stainless steel and simulated the material as a combination of two phases with their own hydrogen diffusion coefficient and solubility. On the interface of both phases, local equilibrium was assumed with consideration of a partitioning constant. In this work, the first model will be used. By comparing this model with the experimental TDS data, insight in the contribution of hydrogen diffusion to TDS curves can be obtained. Hence, the potential impact of hydrogen trapping on experimental TDS curves can be reflected.

Homogeneous hydrogen diffusion was simulated using Fick's 2nd law in its one-dimensional form [31, 63]:

$$\frac{\partial C}{\partial t}(x,t) = D(T(t))\frac{\partial^2 C}{\partial x^2}(x,t). \tag{5.2}$$

With $C(x,t)$, the position (x) and time (t) dependent hydrogen concentration [wppm], D the temperature dependent hydrogen diffusion coefficient [m^2/s], T the temperature [K], t the time [s] and x the position [m]. The diffusion coefficient is thus dependent on the time since temperature and time are linked by the constant applied heating rate. Both charging and discharging processes were simulated to reproduce the experimental TDS profiles. For charging, the initial concentration profile was zero throughout the sample's thickness. The temperature was kept constant. The boundary condition for the charging simulation was

$$C(0,t) = C(d,t) = C_s, \quad t > 0. \tag{5.3}$$

With d the thickness [m] and C_s the equilibrium surface concentration for the given parameters [wppm]. Since the potential did not differ during hydrogen charging, constant concentration boundary conditions were selected. The differential equations were numerically evaluated by Forward-Time-Central-Space finite differentiation (spatial discretion was 6 μm). The time discretion was selected based on the Von Neumann stability criterion, i.e., $0.2 \cdot \frac{\frac{1}{2}dx^2}{\max(D(t))}$ with a maximal value of one second, to assure a precise and stable simulation. For discharging, the concentration profile after charging was used as initial state. The boundary condition for discharging was

$$C(0,t) = Ct(d,t) = 0, \quad t > 0. \tag{5.4}$$

Identical spatial and time discretion were selected as for the charging. To attain a signal that eventually can be compared with the experimental TDS spectra, the flux J [wppm/s] was assessed as

$$J(t) = -\frac{d\overline{C}(t)}{dt} \tag{5.5}$$

with $\overline{C}$ the time-dependent average concentration [wppm]. As discharging involves increasing temperatures, the relationship between the diffusion coefficient and temperature should be incorporated. Turnbull et al. [64] reported $D_{\text{eff}}(t) = 2.8 \cdot 10^{-8} \exp\left(-\frac{39300}{RT(t)}\right)$ m^2/s for 2205 duplex stainless steel. The temperature is linearly related to the time via the applied heating rate. This equation was hence used in the initial simulations.

5.2.4 *Determination of Hydrogen Diffusion Coefficient for Hydrogen Permeation Under Constant Load*

The electrochemical permeation technique was used to determine the hydrogen diffusion coefficient, based on the Devanathan and Stachurski method [65]. A permeation setup was combined with an external loading device (cf. Fig. 5.2). It consisted of two double glass cells with the sample clamped in between. In both cells, a three-electrode system was present, with a working electrode (WE), Pt counter electrode (CE), and Hg/Hg_2SO_4 reference electrode (RE, +650 mV vs. the standard hydrogen electrode, SHE). The three electrodes were connected to a potentiostat in both the cathodic and anodic cell. The temperature of the electrolyte, 0.1 M NaOH in both cells, was kept constant at 25 °C by circulating water in the outer layer of the cells. N_2 gas was blown into the air-tight compartments to reduce the oxygen content and hence minimize unwanted oxidation. The sample's thickness was about 1 mm, as such, hydrogen diffusion was bulk controlled. The methodology is elaborated in more detail in [66].

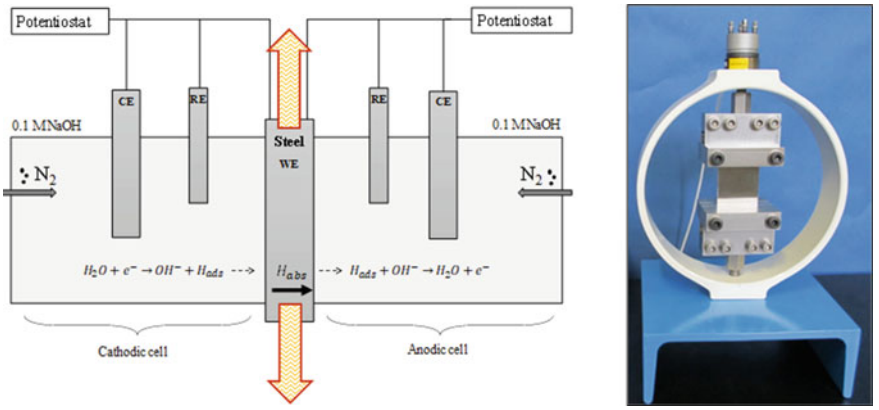

Fig. 5.2 Schematic representation of the electrochemical permeation setup (left) adjusted to allow mechanical loading by a proof ring (right). CE = counter electrode, RE = reference electrode, WE = working electrode (steel) [72] Copyright 2020, Elsevier

It was opted to not apply a Pd layer at the exit side of the sample since during plating process, defects and/or oxides at a metal/Pd interface can be easily introduced. These heterogeneities affect the hydrogen diffusion in an uncontrolled manner, which is not desirable. Moreover, reliable permeation results can be obtained without the use of Pd as well [67–71]. Instead, a passive iron oxide layer was imposed by applying a potential of −500 mV versus RE before starting up the actual experiment. Before this passivation step, the oxygen content in the solution was diminished by blowing N_2 gas through the electrolyte. The anodic cell was filled with the solution by a peristaltic pump and constant circulation was maintained throughout the experiment. Once a stable background current density (<100 nA/cm^2) was achieved, the hydrogen permeation test started, for which the cathodic cell was filled with deaerated NaOH solution under galvanostatic control (−3 mA/cm^2). The hydrogen oxidation current density versus time was then further processed to determine the hydrogen diffusion coefficient, as described below.

To apply a constant load during the in-situ permeation test, the sample was first mounted in the proof ring. Then, the permeation setup was fitted around the specimen. An average thickness of five different measurements in the zone of interest was used to calculate the diffusion coefficient. Hydrogen permeation experiments were performed with a variety of loads on the DP steel. The stress level is expressed as a fraction of the yield strength (YS) and is mentioned in the sample code. Stresses of 60, 80, 100, 120, and 140% of the YS were applied.

The apparent diffusion coefficient ($D_{\text{app,fit}}$) was determined by fitting the theoretical permeation transient, based on Fick's law, with the first half of the normalized permeation transient. This method was selected as the experimental transient started to deviate from the theoretical one at about a normalized current of 0.5. This devi-

ation was clarified by the deposition of metal cations present in the electrolyte, as elaborated elsewhere [66]. Using Fourier series and the right boundary conditions, Fick's 1st and 2nd law could be solved. In this work, the experimental curves were fitted with the galvanostatic model (constant flux, CF) which is expressed by Eq. 5.6 [73, 74]. According to the ASTM international standard, a value of at least n = 6 is recommended [75]. In this work, a value of n = 10 was used.

CF model:

$$\frac{J}{J_\infty} = 1 - \frac{4}{\pi} \sum_{n=0}^{10} \frac{(-1)^n}{2n+1} \exp\left(-\frac{(2n+1)^2 \pi^2 Dt}{4L^2}\right). \tag{5.6}$$

The first step in the fitting procedure was to plot a J_{norm} versus time diagram. This was then fitted to the CF theoretical model. The optimal fit was obtained by minimizing the total error (Eq. 5.7) between the experimental and theoretical curve. Therefore, D was varied using the solver Add-in in Excel.

$$\text{Total error} = \sum \left(\frac{J_{\text{exp}} - J_{\text{back}}}{J_{\text{exp},\infty} - J_{back}} - \frac{J_{\text{th}} - J_{\text{back}}}{J_{\text{th},\infty} - J_{\text{back}}} \right)^2 \tag{5.7}$$

5.2.5 *Determination of the Degree of Hydrogen-Induced Mechanical Degradation*

By comparing mechanical tests performed in air with in-situ tests done on electrochemically hydrogen-charged specimens, the impact of hydrogen on the mechanical performance can be assessed. The samples were electrochemically hydrogen charged by the same method as described above.

At first, the impact of the hydrogen presence on the mechanical behavior of duplex stainless steel was tested by conventional tensile testing. The length direction of the tensile samples was chosen parallel to the rolling direction. Tensile tests were performed at a constant crosshead displacement speed of 0.6 mm/min (strain rate of $1 \cdot 10^{-3} s^{-1}$). Uncharged tests (in air) were done as a reference. Hydrogen-charged tensile specimens were tested in-situ, i.e., with continuous hydrogen charging during the tensile test, after pre-charging for 24 or 168 h. Theoretical calculations of the hydrogen concentration profiles through the thickness of the sample are shown in [58]. These calculations assumed a homogeneous material with one average hydrogen diffusion coefficient and revealed that both charging times did not result in hydrogen saturation. Multiple interrupted tensile tests were done to study the role of hydrogen on the active deformation mechanism of this material, for which both in-situ and ex-situ charging was considered. Furthermore, additional interrupted tensile tests were done, at higher strain levels, to evaluate the initiation and propagation of hydrogen-assisted cracks (HAC). SEM-EBSD was used to study the deformation mechanism and HAC characteristics. The used SEM (FEI QUANTA FEG 450) operated at an

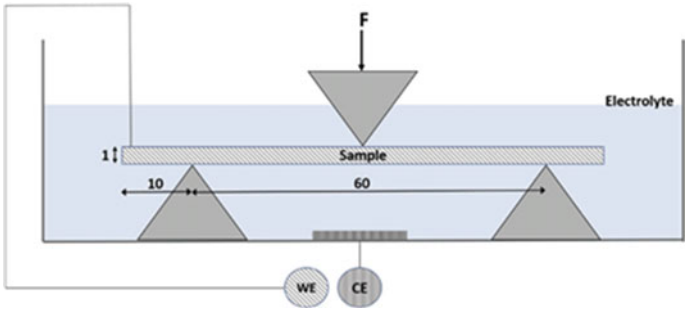

Fig. 5.3 Schematic representation of the in-situ bending technique [60] Copyright 2020, Elsevier

accelerating voltage of 20 kV and a spot size of 5 nm. The specimen was tilted to 70 °C for EBSD measurements. The step sizes used varied between 0.1 and 0.02 μm on a hexagonal grid depending on the used magnification. TSL-OIM Data analysis V7.3 software was used for post-processing and analysis of the crystallographic orientation data.

Secondly, martensitic Fe–C alloys containing a carbon content >0.4 wt% and charged with hydrogen, failed already in the elastic regime during conventional tensile testing [27], as introduced in the introduction part. For these materials with limited ductility, a novel in-situ bending setup was developed to allow the evaluation toward their hydrogen sensitivity. A schematic representation of the setup is presented in Fig. 5.3. During a bending test, a constant transverse loading speed is applied on a beam-shaped sample. The maximum bending stress (σ_{nom}) in a straight beam of height a, thickness B, an applied force F and a moment arm of length z can be calculated by the simple beam theory as

$$\sigma_{\text{nom}} = \frac{6Fz}{Ba^2}. \tag{5.8}$$

However, the validity of this formula is restricted to the elastic regime. In the plastic region, some deviations may occur, but since this work deals with materials with limited ductility, the formula was used for generating both the elastic and plastic region. The bending tests were done for three testing conditions: without hydrogen charging (air), with hydrogen charging during the bending test (in-situ), and pre-charged with hydrogen until saturation and continued in-situ charging during the bending test (saturated in-situ). Two different crosshead deformation speeds (1 mm/min and 0.1 mm/min) were applied. The samples were ground and polished till 1 mm to obtain a defect-free surface and to avoid surface-induced stress concentrations during testing. The samples' thickness was identical for both the mechanical and the hydrogen testing methods, assuring a reliable comparison between the different testing methods.

5.3 The Interaction of Hydrogen with Advanced High-Strength Steels

5.3.1 The Effect of Constant Tensile Load on the Hydrogen Diffusivity of DP Steel by Permeation

A constant tensile load of 60, 80, or 100% of the YS of the DP steel was applied prior to the start of the permeation test. This load sustained during the permeation experiment, corresponding to stress values of 195 MPa, 260 MPa, and 325 MPa, respectively. $D_{app,fit}$, presented in Fig. 5.4a, is obtained by fitting the first half of the normalized current, as elaborated above. The first half of the normalized permeation transients are plotted in Fig. 5.4b. The small scatter can be clarified by the presence of the alumina inclusions, cf. materials characterization section. When comparing the 60%YS and the 80%YS condition, the increased applied load caused an increased diffusivity. Zhao et al. [73] detected a similar increase of D_{app} with imposed elastic stresses. On the one hand, elastic tensile stresses increased the volume of the unit cell and its interstitial sites, which is favorable for hydrogen diffusion [73]. On the other hand, the applied stress increased the hydrogen concentration of the subsurface (C_0). This could also be responsible for the higher $D_{app,fit}$, as an increased $D_{app,fit}$ with increasing C_0 was detected in [76–78]. The cathodic reduction reaction rate at the input surface is higher at a stressed surface leading to a higher hydrogen concentration in the subsurface of the sample.

Though, at 100% of the YS, the diffusivity decreased again reaching similar values as the 0%YS condition (Fig. 5.4a). Since the YS was determined by the 0.2% strain offset method, the stress–strain curve already clearly deviated from the linear elastic part before this determined YS was reached [72]. Moreover, hydrostatic tensile stresses may concentrate surrounding the present inclusions, leading to a local triaxial stress fields where hydrogen can accumulate [28, 57]. As such, some micro-plasticity was locally induced and, correspondingly, dislocations nucleated showing a retardant effect on the diffusivity. The increase in dislocation density with applied (plastic)

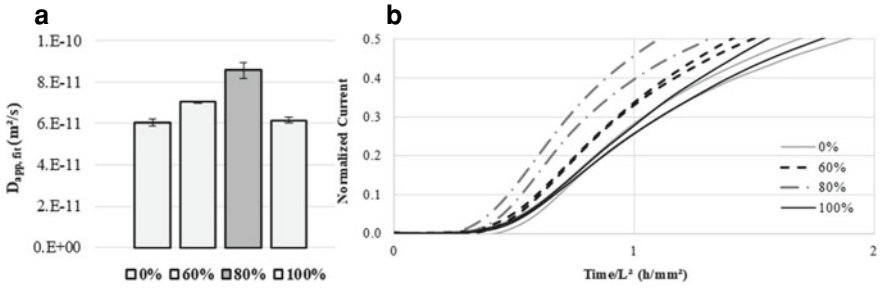

Fig. 5.4 Apparent diffusion coefficients for DP steel under constant elastic stress (% YS), with 0% as reference (**a**). First half of the normalized permeation curves for the different loading conditions (**b**) [72] Copyright 2020, Elsevier

deformation was confirmed in our previous work on this steel grade [39]. Here, it was established that the ferrite grains took most of this plastic deformation. Furthermore, several authors confirmed that dislocations can be considered as hydrogen traps reducing the hydrogen diffusion [79, 80]. This additional trapping compensated for the lattice expansion resulting from the elastic stresses, which are indeed still present as the sample is sustained under constant load. These findings were in agreement with the previously published results, where a decrease in diffusion was observed when applying a stress close or equal to the YS. Again, the generation of microstructural defects by plastic deformation compensated for the lattice expansion [57, 73].

Furthermore, the formation of vacancies and vacancy clusters might also play a role as an increase in vacancy concentration by the annihilation of dislocations during plastic deformation was verified in [81, 82]. Moreover, the formation of vacancies and vacancy clusters is enhanced in the presence of hydrogen [83]. Hydrogen was confirmed by positron annihilation spectroscopy to enhance the generation of vacancies during plastic deformation [84], which was in agreement with TDS data demonstrating an increase in hydrogen absorption by straining [85]. Molecular dynamics and cluster dynamics simulations showed that a hydrogen-vacancy complex is not absorbed by dislocations sweeping through the lattice, unlike a lattice vacancy [86]. When metals undergo plastic deformation in the presence of hydrogen, the simulations demonstrate that the dislocation motion and dislocation–dislocation intersections produce a large amount of hydrogen-vacancy complexes. Under these concentrations, the complexes prefer to grow by absorbing additional vacancies and act as nuclei for nano-voids formation. Vacancies and vacancy clusters are stable and grow easier due to their lower formation energy with the help of trapped hydrogen [87]. These vacancies and vacancy clusters can hinder diffusion by trapping hydrogen as well [88] Therefore, they presumably also contributed to the decreased diffusivity of the 100% YS condition.

The $D_{\mathrm{app,fit}}$ when a constant load in the plastic regime was applied (including the elastic part), are plotted in Fig. 5.5a, including the reference sample, DP0%. The decreased diffusivity, detected for the imposed load of 120 and 140% of the YS, was caused by additional lattice defects induced by increased plastic straining. Consequently, the impact of the plastic stress on the hydrogen diffusion considerably exceeded the effect of the expanded lattice, as both elastic and plastic stresses are present under these loading conditions. The decrease in diffusion due to plastic stresses was also discussed in [89–91]. When a constant load was applied in the plastic regime, self-evidently, the entire contribution of the elastic strain also remained present. As mentioned before, elastic stresses caused a higher diffusivity. Hence, a supplementary proof-of-concept test was designed aiming to separate the contribution of the elastic and plastic stresses. For this purpose, samples were tested by applying a load of 120% of the YS, which was then released (no applied load) prior to the start of the permeation test. As such, the elastic stress contribution was eliminated from the permeation result and only the permanent plastic contribution endured. The related average $D_{\mathrm{app,fit}}$ is indicated in Fig. 5.5b as "120%*". A further reduction in

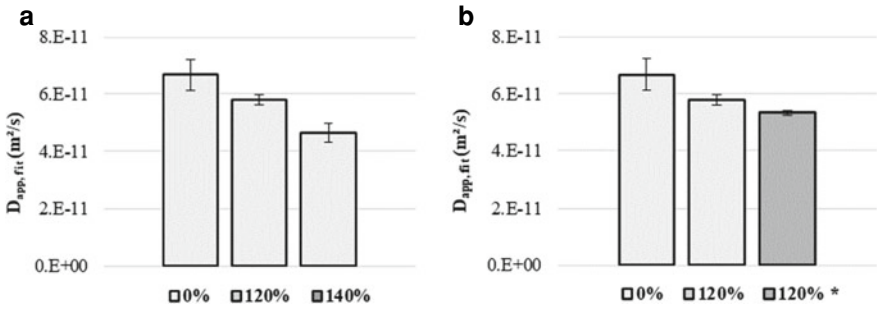

Fig. 5.5 Apparent diffusion coefficients for DP steel under constant applied stress in the plastic regime 120% and 140% YS, with 0% as reference condition (**a**). 120%* was unloaded prior the permeation experiment to confirm the effect of elastic stress (**b**) [72] Copyright 2020, Elsevier

diffusion was observed when the elastic stresses were eliminated. This demonstrated once more that elastic stresses caused a higher diffusion, whereas the microstructural changes by plastic deformation accounted for a decrease in diffusivity.

5.3.2 Revealing the Role of Hydrogen in Duplex Stainless Steels

5.3.2.1 Critical Assessment of Hydrogen Trapping of Duplex Stainless Steel Evaluated by TDS

Figure 5.6 present the hydrogen uptake capacity versus applied charging time by melt extraction tests, including the fit of the analytical solution of Fick's 2nd law. The saturation level of this material was about 702 wppm. The effective diffusion coefficient was determined to be $9.94 \cdot 10{-}15$ m^2/s, which is in good agreement with literature [92, 93]. Figure 5.7 shows the obtained TDS data; both fast heating rates (600 and 900 K/h, cf. Fig. 5.7a) and slow heating rates (20, 35 and 50 K/h, cf. Fig. 5.7b) were applied. The latter because of a potential enhanced peak separation between diffusion and trapping processes. The spectra of the samples charged for 15 days showed a different shape, dependent on the applied heating rate. The fast heating rates (15d H) resulted in one asymmetric peak with a rather flat top. The slow heating rates (15d H) caused a small peak followed by a two-step peak. The samples charged for 1 day (1d H) revealed one main peak followed by a shoulder finishing at about the same temperature as the corresponding 15 days charged sample. This was observed for both the fast and slow heating rates. However, the 1 day charged specimen tested at 50 K/h showed an additional small peak in the beginning as was also the case for the 15 days charged sample at this heating rate (cf. Fig. 5.7b).

The desorption activation energy was determined based on the experimental data, as described above, and resulted in an average E_a of 43.4 kJ/mol. This experimen-

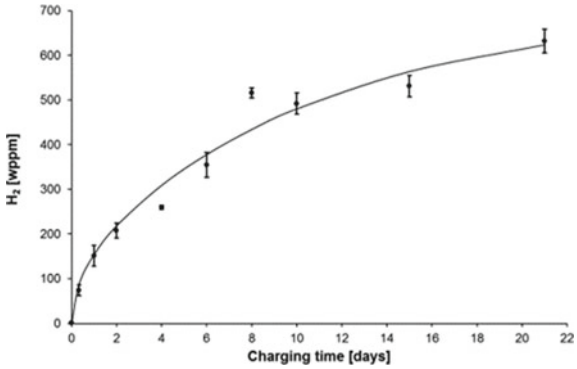

Fig. 5.6 Hydrogen content versus charging time with fit based on analytical solution of Fick's 2nd law [62] Copyright 2020, Elsevier

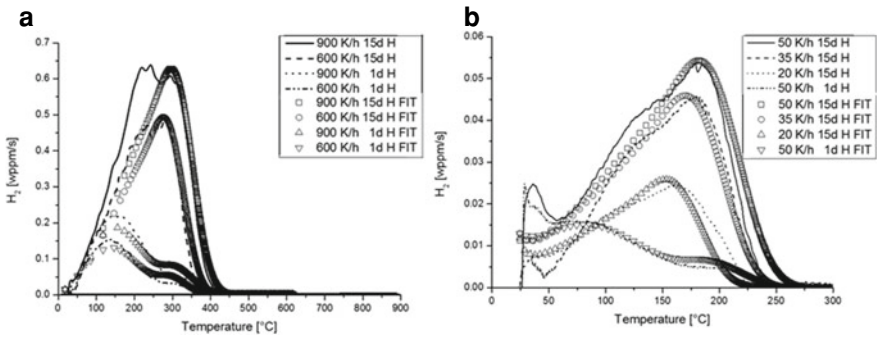

Fig. 5.7 TDS data of 2205 duplex stainless steel for different charging times and heating rates (fast in (**a**), slow in (**b**)). Fit of the homogeneous diffusion model to the experimental TDS data included [62] Copyright 2020, Elsevier

tally obtained diffusion activation energy was then implemented in the homogeneous model. The pre-exponential factor was determined by visual correspondence with the experimental data. This resulted in an expression for the effective diffusion coefficient $D_{\text{eff}} = 3 \cdot 10^{-7} \cdot \exp(-\frac{43400}{RT})$. The obtained fits are included in Fig. 5.7. The numerical analysis exposed that the shape of the curves can be clarified by hydrogen diffusion processes only. An asymmetric shape arose for homogeneously charged samples, caused by the increasing diffusion upon increasing temperature. Similar shapes were experimentally observed when duplex stainless steels were homogeneously charged by gaseous charging [94, 95].

An average diffusion activation energy was determined based on the experimental data with a value in between diffusion in ferrite and austenite. Since the value is rather close to the one of austenite, it can be stated that most hydrogen diffused through several austenitic layers during leaving the sample. Hydrogen trapping in ferrite was not visible from the experimental results. Hydrogen atoms that are released from traps

in ferrite are overruled by the large amount of hydrogen atoms that are released from austenite, i.e., the austenite diffusion peak overlaps with the peaks related to trapping in ferrite. Pu et al. [96] also argued that traps created through deformation of 304 stainless steel (dislocations and martensite) cannot be viewed in the large amount of hydrogen originating from interstitial positions in austenite. Evaluation of hydrogen trapping in duplex stainless steels appeared not to be possible as was shown by combining experimental results with diffusion models. Microstructural features with desorption activation energies greater than the diffusion activation energy of austenite can presumably be distinguished as a shoulder on TDS curves; however, they were not observed in the duplex stainless steel studied in this work. Hydrogen desorbing from austenite by diffusion determined completely the shape of the experimental TDS spectra. The main effect of the presence of the ferrite phase was an increase of the average diffusion kinetics.

5.3.2.2 Impact of Hydrogen on Active Deformation Mechanism of Duplex Stainless Steels

Figure 5.8 presents the EBSD measurements on the normal direction (ND) surface of the interrupted tensile tests in air (b), and for ex-situ (c) and in-situ (d) hydrogen-charged specimen. The initial condition, without hydrogen charging and deformation, is included as reference (a). Both image quality maps and phase maps are shown. Figure 5.9 displays a detailed EBSD measurement of a deformed austenite grain on the interrupted in-situ hydrogen-charged specimen. An image quality map, inverse pole figure (IPF) map and phase map are presented in this case. Moreover, several pole figures are included of specific crystallographic directions versus the sample reference system. These were constructed by first creating a partition based on crystal orientation with a maximal deviation of 5 °C. The orientations are indicated on the IPF map. High angle grain boundaries (>15 °C) are indicated in black in both figures.

Planar slip and both ε- and α'-martensite were detected in the austenite phase of the hydrogen-charged specimens being more noticeable for in-situ compared to ex-situ tensile testing. Both phenomena were absent for uncharged specimens. This could be clarified by a reduction in SFE, complemented by a change in what phase is accommodating most of the plastic deformation. Besides, additional pinning of edge dislocations by hydrogen atmospheres hindering cross-slip contributed to the difference in deformation mechanism. Hydrogen-induced martensitic transformations took place soon after yielding and were mainly characterized as ε-martensite. When higher strain levels were reached, hydrogen-assisted cracks initiated [97]. These HACs were studied with SEM-EBSD to identify the microstructurally most prone regions. Figure 5.10a shows an image of several cracks. The initiation characteristics were identified based on the phase map (cf. Fig. 5.10b) and ND IPF map (cf. Fig. 5.10c). The phase maps designated in which phase the crack initiated, whereas the ND IPF maps indicated whether the crack initiated on a grain boundary or inside a grain. Cracks, small enough to stay within one phase or boundary, were used for the statistic determination of the most favorable initiation site. Different categories

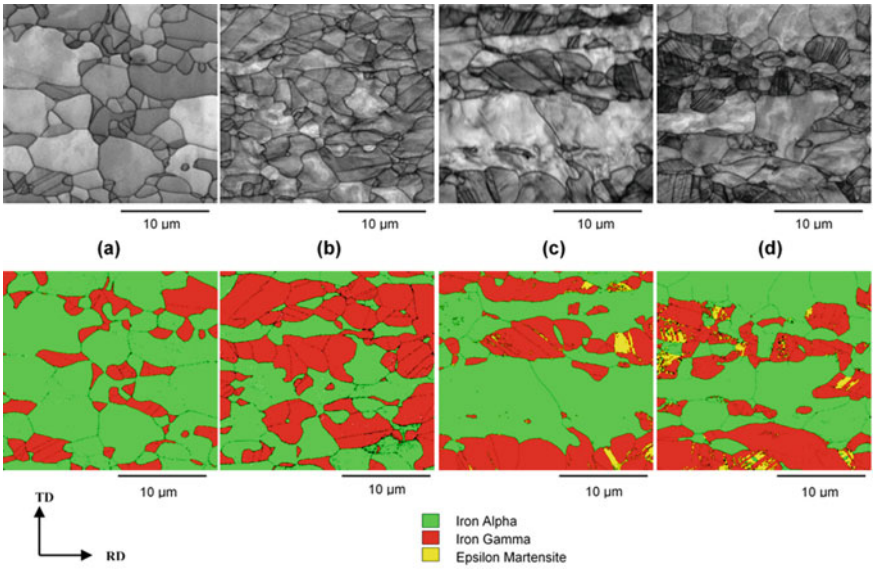

Fig. 5.8 EBSD measurements showing image quality and phase map on **a** initial state, **b** interrupted tensile test in air, **c** ex-situ interrupted tensile test and **d** in-situ interrupted tensile test [58] Copyright 2019, Elsevier

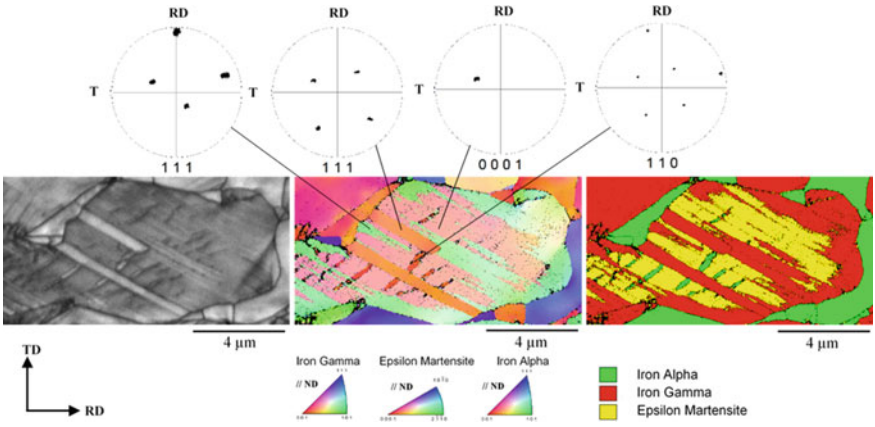

Fig. 5.9 Detailed EBSD measurement on hydrogen charged and in-situ deformed austenite grain. Various pole figures are included [58] Copyright 2019, Elsevier

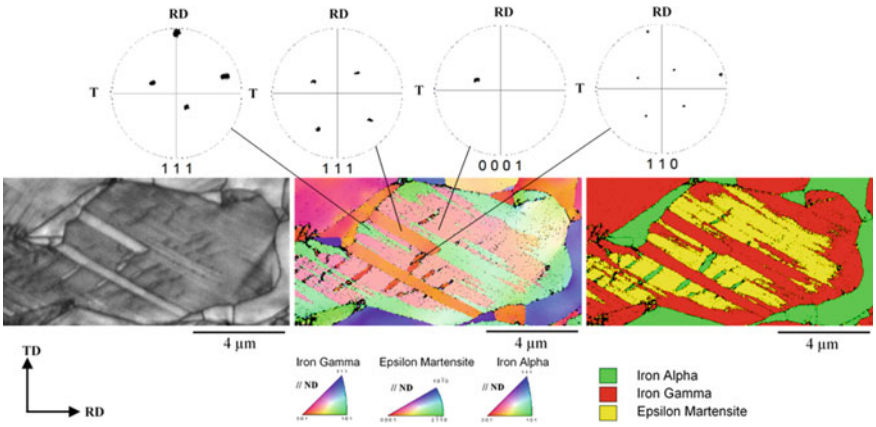

Fig. 5.10 EBSD characterization of HACs on ND plane after straining hydrogen-charged (1 day) duplex stainless steel to an intermediate elongation. **a** SEM image with type of crack (A = austenite, F = ferrite, M = martensite, IF = interface and GB = grain boundary), **b** phase map and (**c**) ND IPF map [97] Copyright 2020, Elsevier

were chosen; austenite grain interior, austenite/austenite grain boundary, austenite/martensite interface, ferrite grain interior or austenite/ferrite interface. The larger part (78.7%) of the cracks initiated in austenite (including the grain interior, grain boundaries of two adjacent austenitic grains and the austenite/martensite interface), followed by ferrite (16.6%) and finally the interface between austenite and ferrite (4.7%).

5.4 The Interaction of Hydrogen with Lab Cast Fe–C Alloys

In this section, a new in-situ bending technique is used to study the fracture mechanism of high-strength steels with limited ductility in the presence of hydrogen. The methodology was tested for generic Fe–C steels with a carbon content of 0.2, 0.4, and 1.1 wt.%. Figure 5.11a shows the hydrogen uptake capacity versus applied charging time, termed hydrogen saturation curves. The maximal amount of absorbed hydrogen increased with increasing carbon content. Fe–0.4C required longer charging times to reach hydrogen saturation than the Fe–0.2C due to a reduced hydrogen diffusivity. For the Fe–1.1C alloy, saturation is never reached. This can be attributed to the interaction between hydrogen with the present quench cracks in this material (cf. Fig. 5.1). Hydrogen charging caused additional cracking in this material [60]. However, for bending experiments with "saturated" samples, a charging time of two hours was chosen. No hydrogen-induced damage was observed for the other two materials. Figure 5.11b shows the bending curves of the Fe–0.4C samples. Although

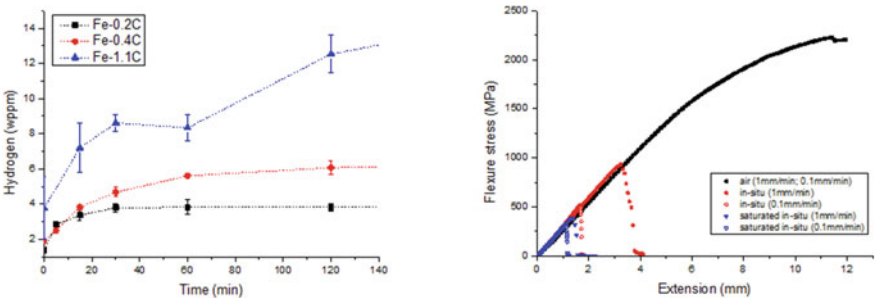

Fig. 5.11 Hydrogen saturation curves for the Fe–C alloys (**a**). Bending curves of Fe–0.4C, tested at 1 mm/min and 0.1 mm/min for different testing conditions (air, in-situ charged and in-situ charged after hydrogen pre-charging until saturation (cf. data shown in (**a**)) [60] Copyright 2020, Elsevier

Fe–0.4C samples are too brittle to be tested in tensile loading [27], they possess enough ductility for bending. In Fig. 5.11, the bending curves are only shown up to 12 mm of extension since from this point onward the support points change and there is a transition from three-point bending to four-point bending. Three different test conditions were compared; i.e., air, in-situ and saturated (pre-charged) in-situ, as described above. When the samples were charged with hydrogen, the flexure stress clearly decreased and fracture occurred abruptly. This effect is more pronounced when the samples were exposed to hydrogen for longer times, i.e., slower applied strain rates and/or with pre-charging. When the bending rate was decreased, hydrogen had more time to diffuse toward the highly stressed regions linked to the fracture initiation/propagation sites. When the samples were pre-charged, all the available trapping sites are occupied by hydrogen, and hydrogen can internally redistribute to the highly stressed parts and facilitate fracture. Due to these two factors, the sensitivity to failure increased for pre-charged samples and when lowering the bending deformation speed. The hydrogen embrittlement effect can be visualized by analyzing the related fracture surfaces by SEM. Figure 5.12 shows an overview of the appearance of the fracture surfaces for each testing condition.

In the absence of hydrogen, intergranular features and microvoids characterized the fracture surface. When the bending test was done with simultaneous hydrogen charging, additional cleavage facets, and cracks were found. When the in-situ test was done at a slower strain rate, the microvoids disappeared and the fracture surface was a mixture of intergranular and cleavage aspects accompanied with cracks. A similar fracture surface was detected when the sample was saturated before the test at 1 mm/min, although the cleavage fraction increased. Finally, when the sample was saturated and tested at lower strain rate, a transition to a pure cleavage fracture with dispersed cracks was seen. When hydrogen is added, the fracture mechanism changed since cracks perpendicular to the fracture surface were observed and the plastic strain marks almost completely disappeared. These perpendicular cracks run transgranular both along and through martensitic blocks (cf. Fig. 5.13b). The direction of the crack propagation changed with the orientation of the martensitic laths, indicating that

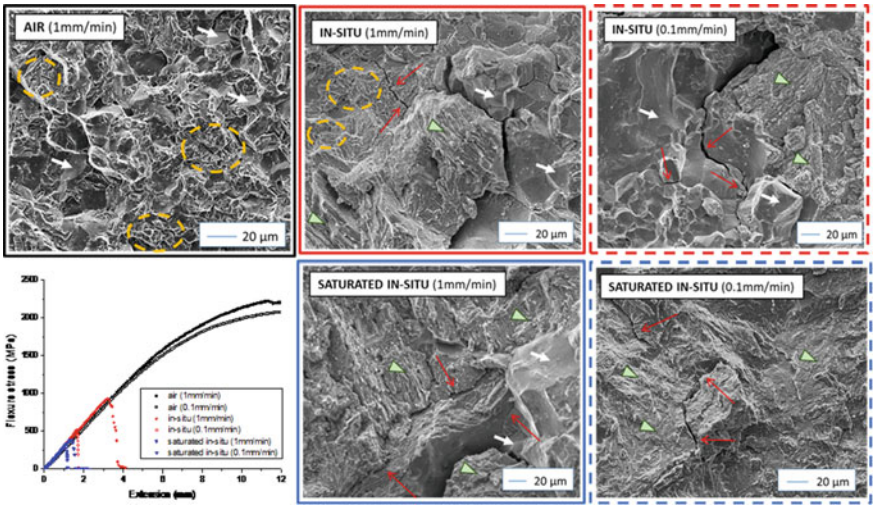

Fig. 5.12 SEM characterization of the fracture surfaces of Fe–0.4C for different conditions; air, in-situ, and saturated in-situ. Yellow dotted circles indicate zones with microvoids, white arrows intergranular features and green arrowheads cleavage features. Cracks are illustrated by fine red arrows [60] Copyright 2020, Elsevier

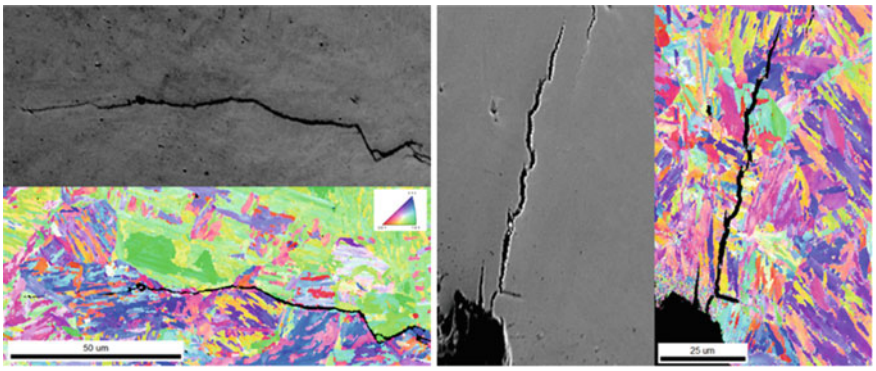

Fig. 5.13 EBSD scan of a crack running parallel to the fracture surface of Fe–0.4C subjected to bending in air (**a**), and a crack running perpendicular to the fracture surface in the presence of hydrogen (**b**) [60] Copyright 2020, Elsevier

cracks preferably ran along block boundaries. This is not the case in the air samples, where the crack propagated along the prior austenite grain boundaries (cf. Fig. 5.13a). Therefore, it can be stated that hydrogen weakened the block boundaries, which explained the shift to a cleavage type of fracture when hydrogen is present. As suggested by Nagao et al. [98], this quasi-cleavage fracture mode is a result of localized plasticity and a local hydrogen overconcentration at packet and/or block boundaries, which are high angle grain boundaries (HAGBs). On the one hand, HAGBs hinder dislocation movement causing a dislocation pile-up at the boundary.

On the other hand, HAGBs are effective hydrogen traps resulting in a decrease of the cohesive forces. These two phenomena weaken the block boundaries, causing quasi-cleavage features. This mechanism is termed "Hydrogen Enhanced Plasticity Mediated Decohesion". It can be considered as a mixture of HELP and HEDE, i.e., hydrogen activates different slip systems (HELP) which can intersect HAGBs and enhances hydrogen distribution by dislocations. This causes an increased amount of hydrogen deposited at the HAGBs which in turn weakens the cohesive forces at these boundaries (HEDE).

Hydrogen caused a noteworthy ductility loss, described by a transition from a microvoid (Fe–0.2C), intergranular (Fe–1.1C), or mixed (Fe–0.4C) fracture appearance to a cleavage type of fracture with additional cracking. The transition to the transgranular fracture type was explained by the Hydrogen Enhanced Plasticity Mediated Decohesion model. The similarities in the fracture mechanism for these alloys acknowledges the developed in-situ bending technique as a suitable method to evaluate the susceptibility to hydrogen embrittlement of high-strength steels.

5.5 Conclusion

This work provides an overview of our recent work on dedicated experimental methodologies to reveal specific aspects of the interaction of hydrogen with a steel microstructure. Firstly, the effect of constant tensile load on the hydrogen diffusivity was evaluated by electrochemical hydrogen permeation experiments during in-situ constant loading on DP steel. Secondly, a critical assessment of the evaluation of hydrogen trapping of low hydrogen diffusion materials was performed for duplex stainless steels. Moreover, the effect of hydrogen on the active deformation mechanism in this material was demonstrated as well by interrupted in-situ tensile tests combined with SEM-EBSD. Finally, the sensitivity of high strength-low ductility steels to hydrogen embrittlement was evaluated by in-situ bending tests. The operational embrittlement mechanism in these alloys was proposed based on SEM fractography. Key takeaways of this work are

1. Elastic applied tensile stresses increased the hydrogen diffusivity of DP steel due to the volume increase of the unit cell. When the imposed stress was equal to the yield stress, the increasing amount of hydrogen traps compensated for the increase of the diffusion coefficient resulting from the lattice expansion. Significant plastic deformation slowed down the diffusion due to the formation of lattice defects such as dislocations, vacancies, and vacancy clusters.
2. A combined experimental and numerical approach was used to increase the insights on the interpretation of TDS data of duplex stainless steel. It was verified that hydrogen desorbed through diffusion with an experimentally obtained value for the effective hydrogen diffusion coefficient in between the hydrogen diffusion coefficients in ferrite and austenite.
3. Planar slip and both ε- and α'-martensite were detected in the austenite phase of the hydrogen-charged duplex stainless steel specimens. This was more pronounced for in-situ compared to ex-situ tensile testing. Both phenomena were

absent in the uncharged condition. This was explained by a reduction in SFE together with a change in which phase accommodated most of the plastic deformation. Besides, additional pinning of edge dislocations by hydrogen atmospheres contributed to the large difference in observed deformation mechanism as well. At higher strain levels, hydrogen-assisted cracks initiated. Statistical analysis based on EBSD confirmed that the largest fraction of these cracks initiated in austenite.

4. The fracture mechanism in the presence of hydrogen for high strength-low ductility Fe–C steels was evaluated by in-situ bending. Hydrogen caused a noteworthy ductility loss, characterized by a transition from a microvoid (Fe–0.2C), intergranular (Fe–1.1C) or mixed (Fe–0.4C) fracture surface to a cleavage fracture surface with additional cracking. The transition to the transgranular fracture type is clarified by the Hydrogen Enhanced Plasticity Mediated Decohesion model, indicating that hydrogen was preferentially trapped at packet or block boundaries, causing a cleavage type of fracture.

Acknowledgements The authors wish to thank the senior postdoctoral fellowship of the Research Foundation-Flanders (FWO) via grant 12ZO420N and the Special Research Fund (BOF), UGent (grants BOF01P03516, BOF15/BAS/062 and BOF/01J06917) for support. Special thanks goes to Dr. E. Van den Eeckhout, L. Claeys and M. Pinson for their valuable contribution to the results presented in this chapter. The authors also acknowledge the technical staff from the Department Materials, Textiles and Chemical Engineering, UGent, for their help with the experiments and/or sample preparation.

References

1. Woodtli, J., Kieselbach, R.: Damage due to hydrogen embrittlement and stress corrosion cracking. Eng. Fail. Anal. **7**, 427–450 (2000)
2. Hilditch, T., Lee, S., Speer, J., Matlock, D.: Response to hydrogen charging in high strength automotive sheet steel products. SAE Technol. Paper (2003). https://doi.org/10.4271/2003-01-0525
3. Venezuela, J., Liu, Q., Zhang, M., Zhou, Q., Atrens, A.: The influence of hydrogen on the mechanical and fracture properties of some martensitic advanced high strength steels studied using the linearly increasing stress test. Corros. Sci. **99**, 98–117 (2015)
4. Depover, T., Escobar, D., Wallaert, E., Zermout, Z., Verbeken, K.: Effect of hydrogen charging on the mechanical properties of advanced high strength steels. Int. J. Hydrog. Energy **39**, 4647–4656 (2014)
5. Olden, V., Thaulow, C., Johnsen, R., Ostby, E., Berstad, T.: Influence of hydrogen from cathodic protection on the fracture susceptibility of 25%Cr duplex stainless steel - Constant load SENT testing and FE-modelling using hydorgen influenced cohersive zone elements. Eng. Fract. Mech. **76**, 827–844 (2009)
6. Johnson, W.: On some remarkable change produced in iron and steel by the action of hydrogen and acids. Proc. R. Soc. Lond. **23**, 168–179 (1875)
7. Hirth, J.: Effects of hydrogen on the properties of iron and steel. Metall. Trans. A **11A**, 861–890 (1980)
8. Oriani, R., Hirth, J., Smialowski, M.: Hydrogen Degradation of Ferrous Alloys. Noyes Publications, New Jersey (1985)

9. Sofronis, P.: Special issue on recent advances in engineering aspects of hydrogen embrittlement. Eng. Fract. Mech. **68**, 617–617 (2001)
10. Pundt, A., Kirchheim, R.: Hydrogen in metals: microstructural aspects. Ann. Rev. Mater. Res. **36**, 555–608 (2006)
11. Somerday, B., Sofronis, P., Jones, R. (eds.): Effects of Hydrogen on Materials. Wyoming, USA (2008)
12. Somerday, B., Sofronis, P., Jones, R. (eds.): Hydrogen-Materials Interactions. Wyoming, USA (2012)
13. Gangloff, P., Somerday, B.: Gaseous Hydrogen Embrittlement of Materials in Energy Technologies. Woodhead, Cambridge (2012)
14. Somerday, B., Gangloff, P., Jonas, R. (eds.): Effects of Hydrogen on Materials. Wyoming, USA (2016)
15. Revie, R., Sastri, V., Elboujdaii, M., Ramsingh, R., Lafrenière, Y.: Hydrogen-induced cracking of line pipe steels used in sour service. Corros. **49**, 531–536 (1993)
16. Maroef, I., Olson, D., Eberhart, M., Edwards, G.: Hydrogen trapping in ferritic steel weld metal. Int. Mater. Rev. **47**, 191–223 (2002)
17. Olden, V., Saai, A., Jemblie, L., Johnsen, R.: FE simulation of hydrogen diffusion in duplex stainless steel. Int. J. Hydrog. Energy **39**, 1156–1163 (2014)
18. Troiano, A.: The role of hydrogen and other interstitials in the mechanical behaviour of metals. Trans. ASM **52**, 54–80 (1960)
19. Beachem, C.: A new model for hydrogen-assisted cracking. Metall. Mater. Trans. B **3**, 441–455 (1972)
20. Lynch, S.: Comments on "A unified model of environment-assisted cracking". Scr. Mater. **61**, 331–334 (2009)
21. Lynch, S.: Environmentally assisted cracking: overview of evidence for an adsorption-induced localised-slip process. Acta Metall. **36**, 2639–2661 (1988)
22. Nagumo, M.: Hydrogen related failure of steels—a new aspect. Mater. Sci. Technol. **20**, 940–950 (2004)
23. Gangloff, R.: Hydrogen assisted cracking of high strength alloys. In: Mine, I., Ritchie, R., Karihaloo, B. (eds.) Comprehensive Structural Integrity, pp. 31–101. Elsevier, Amsterdam (2003)
24. Barnoush, A., Vehoff, H.: Electrochemical nanoindentation: a new approach to prove hydrogen/deformation interaction. Scr. Mater. **55**, 195–198 (2006)
25. Birnbaum, H., Sofronis, P.: Hydrogen-enhanced localized plasticity—a mechanism for hydrogen-related fracture. Mater. Sci. Eng. A **176**, 191–202 (1994)
26. Depover, T., Wallaert, E., Verbeken, K.: Fractographic analysis of the role of hydrogen diffusion on the hydrogen embrittlement susceptibility of DP steel. Mater. Sci. Eng. A **649**, 201–208 (2016)
27. Depover, T., Wallaert, E., Verbeken, K.: On the synergy of diffusible hydrogen content and hydrogen diffusivity in the mechanical degradation o flaboratory cast Fe-C alloys. Mater. Sci. Eng. A **664**, 195–205 (2016)
28. Depover, T., Hertelé, S., Verbeken, K.: The effect of hydrostatic stress on the hydrogen induced mechanical degradation of dual phase steel: A combined experimental and numerical approach. Eng. Fract. Mech. **221**, 106704 (2019)
29. Depover, T., Verbeken, K.: The detrimental effect of mobile hydrogen at dislocations on the hydrogen embrittlement susceptibility of Fe-C-X alloys: an experimental proof of the HELP mechanism. Int. J. Hydrog. Energy **43**, 3050–3061 (2018)
30. Depover, T., Verbeken, K.: The effect of TiC on the hydrogen induced ductility loss and trapping behavior of Fe-C-Ti alloys. Corros. Sci. **112**, 308–326 (2016)
31. Kirchheim, R.: Bulk diffusion-controlled thermal desorption spectroscopy with examples for hydrogen in iron. Metall. Mater. Trans. A **47A**, 672–696 (2016)
32. Nagumo, M., Takai, K.: The predominant role of strain-induced vacancies in hydrogen embrittlement of steels: overview. Acta Mater. **165**, 722–733 (2019)

33. Kissinger, H.: Reaction kinetics in differential thermal analysis. Anal. Chem. **29**, 1702–1706 (1957)
34. Lee, J., Lee, J.: Hydrogen trapping in AISI-4340 steel. Metall. Sci. **17**, 426–432 (1983)
35. Lee, J., Lee, S.: Hydrogen trapping phenomena in metals with BCC and FCC crystal structures by the desorption thermal-analysis technique. Surf. Coat. Technol. **28**, 301–314 (1986)
36. Lee, S., Lee, J.: The trapping and transport phenomena of hydrogen in nickel. Metall. Trans. A **17A**, 181–187 (1986)
37. Verbeken, K.: Analysing hydrogen in metals: bulk thermal desorption spectroscopy (TDS) methods. In: Gangloff, P., Somerday, B. (eds.) Gaseous Hydrogen Embrittlement of Materials in Energy Technologies, pp. 27–55. Woodhead, Cambridge (2012)
38. Oriani, R.: The diffusion and trapping of hydrogen in steel. Acta Metall. **18**, 147–157 (1970)
39. Depover, T., Hajilou, T., Wan, D., Wang, D., Barnoush, A., Verbeken, K.: Assessment of the potential of hydrogen plasma charging as compared to conventional electrochemical hydrogen charging on dual phase steel. Mater. Sci. Eng. A **754**, 613–621 (2019)
40. Thomas, L., Li, D., Gangloff, R., Scully, J.: Trap-governed hydrogen diffusivity and uptake capacity in ultrahigh strength AERMET 100 steel. Metall. Mater. Trans. A **33**, 1991–2004 (2002)
41. Choo, W., Lee, J.: Thermal analysis of trapped hydrogen in pure iron. Metall. Mater. Trans. A **13**, 135–140 (1982)
42. Pressouyre, G.: Classification of hydrogen traps in steel. Metall. Trans. A **10A**, 1571–1573 (1979)
43. Di Stefano, D., Nazarov, R., Hickel, T., Neugebauer, J., Mrovec, M., Elsässer, C.: First principles investigation of hydrogen interaction with TiC precipitates in alpha-Fe. Phys. Rev. **93**, 184108–1–14 (2016)
44. Depover, T., Verbeken, K.: Evaluation of the effect of V4C3 precipitates on the hydrogen induced mechanical degradation in Fe-C-V alloys. Mater. Sci. Eng. A **675**, 299–313 (2016)
45. Drexler, A., Depover, T., Verbeken, K., Ecker, W.: Model-based interpretation of thermal desorption spectra of Fe-C-Ti alloys. J. Alloys Compd. **789**, 647–657 (2019)
46. Drexler, A., Depover, T., Leitner, S., Verbeken, K., Ecker, W.: Microstructural based hydrogen diffusion and trapping models applied to Fe-C-X alloys. J. Alloys Compd. **826**, 154057 (2020)
47. Wei, F., Hara, T., Tsuzaki, K.: Precise determination of the activation energy for desorption of hydrogen in two Ti-added steels by a single thermal-desorption spectrum. Metall. Mater. Trans B **35**, 587–597 (2004)
48. Depover, T., Verbeken, K.: Evaluation of the role of Mo2C in hydrogen induced ductility loss in Q&T Fe-C-Mo alloys. Int. J. Hydrog. Energy **41**, 14310–14329 (2016)
49. Sun, X., Xu, J., Li, Y.: Hydrogen permeation behaviour in austenitic stainless steel. Mater. Sci. Eng. A **114**, 179–187 (1989)
50. Laureys, A., Depover, T., Petrov, R., Verbeken, K.: Microstructural characterization of hydrogen induced cracking in TRIP-assisted steel by EBSD. Mater. Charact. **112**, 169–179 (2016)
51. Laureys, A., Pinson, M., Depover, T., Petrov, R., Verbeken, K.: EBSD characterization of hydrogen induced blisters and internal cracks in TRIP-assisted steel. Mater. Charact. **159**, 110029 (2020)
52. Laureys, A., Depover, T., Petrov, R., Verbeken, K.: Characterization of hydrogen induced cracking in TRIP-assisted steels. Int. J. Hydrog. Energy **40**, 16901–16912 (2015)
53. Depover, T., Wan, D., Wang, D., Barnoush, A., Verbeken, K.: The effect of hydrogen on the crack initiation site of TRIP-assisted steels during in-situ hydrogen plasma micro-tensile testing: Leading to an improved ductility. Mater. Charact. **167**, 110493 (2020)
54. Koyama, M., Tasan, C., Akiyama, E., Tsuzaki, K., Raabe, D.: Hydrogen-assisted decohesion and localized plasticity in dual-phase steel. Acta Mater. **70**, 174–187 (2014)
55. Liu, Q., Zhou, Q., Venezuela, J., Zhang, M., Atrens, A.: The role of the microstructure on the influence of hydrogen on some advanced high-strength steels. Mater. Sci. Eng. A **715**, 370–378 (2018)

56. Tasan, C., Diehl, M., Yan, D., Bechtold, M., Roters, F., Schemmann, L., Zheng, C., Peranio, N., Ponge, D., Koyama, M., Tsuzaki, K., Raabe, D.: An overview of dual phase steels: advances in microstructure-oriented processing and micromechanical guided design. Ann. Rev. Mater. Res. **45**, 391–431 (2015)
57. Kim, S., Yun, D., Jung, H., Kim, K.: Determination of hydrogen diffusion parameters of ferritic steel from electrochemical permeation measurement under tensile loads. J. Electrochem. Soc. **161**, 173–181 (2014)
58. Claeys, L., Depover, T., De Graeve, I., Verbeken, K.: First observation by EBSD of martensitic transformations due to hydrogen presence during straining of duplex stainless steel. Mater. Charact. **156**, 109843 (2019)
59. Claeys, L., Depover, T., De Graeve, I., Verbeken, K.: Electrochemical hydrogen charging of duplex stainless steel. Corros. **75**, 880–887 (2019)
60. Pinson, M., Springer, H., Depover, T., Verbeken, K.: Qualification of the in-situ bending technique towards the evaluation of the hydrogen induced fracture mechanism of martensitic Fe-C steels. Mater. Sci. Eng. A **792**, 139754 (2020)
61. Marder, A., Benscoter, A., Krauss, G.: Microcracking sensitivity in Fe-C plate martensite. Metall. Trans. **1**, 1545–1549 (1970)
62. Claeys, L., Cnockaert, V., Depover, T., De Graeve, I., Verbeken, K.: Critical assessment of the evaluation of thermal desorption spectroscopy data for duplex stainless steels: A combined experimental and numerical approach. Acta Mater. **186**, 1–9 (2020)
63. Crank, J.: The Mathematics of Diffusion. Clarendon Press, Oxford (1975)
64. Turnbull, A., Beylegaard, E., Hutchings, R.: Hydrogen transport in SAF 2205 and SAF 2507 duplex stainless steels. In: Turnbull, A. (ed.) Hydrogen Transport and Cracking in Metals, pp. 268–279. Woodhead, Cambridge (1994)
65. Devanathan, M., Stachurski, Z.: The adsorption and diffusion of electrolytic hydrogen in palladium. Proc. R. Soc. A **270**, 90–101 (1962)
66. Van den Eeckhout, E.: Methodological Study of the Hydrogen Diffusion in Steel by Means of Electrochemical Permeation. Ghent University, Ghent (2019)
67. Frappart, S.: Des éléments de compréhension sur les mécanismes de transport et de ségrégation de l'hydrogéne dans les aciers martensitiques trempés et revenus á haute limite d'élasticité. Université de La Rochelle, La Rochelle (2011)
68. Collet-Lacoste, J.: Intervention des phenomenes de surface sur la permeation electrochimique de l'hydrogene dans le fer: Role d'une couche d'oxyde ou de palladium. Université de Paris-Sud Centre d'Orsay, Paris (1993)
69. Pyun, S., Oriani, R.: The permeation of hydrogen through the passivating films on iron and nickel. Corros. Sci. **29**, 485–496 (1989)
70. Van den Eeckhout, E., Depover, T., Verbeken, K.: The effect of microstructural characteristics on the hydrogen permeation transient in quenched and tempered martensitic alloys. Metals **8**, 779 (2018)
71. Depover, T., Van den Eeckhout, E., Verbeken, K.: The impact of hydrogen on the ductility loss of bainitic Fe-C alloys. Mater. Sci. Technol. **32**, 1625–1631 (2016)
72. Van den Eeckhout, E., De Baere, I., Depover, T., Verbeken, K.: The effect of a constant tensile load on the hydrogen diffusivity in dual phase steel by electrochemical permeation experiments. Mater. Sci. Eng. A **773**, 138872 (2020)
73. Zhao, W., Zhang, T., He, Z., Sun, J., Wang, Y.: Determination of the critical plastic strain-induced stress of X80 steel through an electrochemical hydrogen permeation method. Electrochem. Acta **214**, 336–344 (2016)
74. Owczarek, E., Zakroczymski, T.: Hydrogen transport in a duplex stainless steel. Acta Mater. **48**, 3059–3070 (2000)
75. ASTM G148-97, Standard Practice for Evaluation of Hydrogen Uptake, Permeation, and Transport in Metals by an Electrochemical Technique (2011)
76. Frappart, S., Feaugas, X., Creus, J., Thebault, F., Delattre, L., Marchebois, H.: Study of the hydrogen diffusion and segregation into Fe-C-Mo martensitic HSLA steel using electrochemical permeation test. J. Phys. Chem. Solids **71**, 1467–1479 (2010)

77. Turnbull, A.: Perspectives on hydrogen uptake, diffusion and trapping. Int. J. Hydrog. Energy **40**, 16961–16970 (2015)
78. Namboodhiri, T., Nanis, L.: Concentration dependence of hydrogen diffusion in Armco iron. Acta Metall. **21**, 663–672 (1973)
79. Kumnick, A., Johnson, H.: Hydrogen transport through annealed and deformed Armco iron. Metall. Trans. **5**, 1199–1206 (1974)
80. Van den Eeckhout, E., Laureys, A., Van Ingelgem, Y., Verbeken, K.: Hydrogen permeation through deformed and heat-treated Armco pure iron. Mater. Sci. Technol. **33**, 1515–1523 (2017)
81. Essmann, U., Mughrabi, H.: Annihilation of dislocations during tensile and cyclic deformation and limits of dislocation densities. Philos. Mag. A **40**, 731–756 (1979)
82. Ohashi, T.: Generation and accumulation of atomic vacancies due to dislocation movement and pair annihilation. Philos. Mag. **98**, 2275–2295 (2018)
83. Doshida, T., Suzuki, H., Takai, K., Oshima, N., Hirade, T.: Enhanced lattice defect formation associated with hydrogen and hydrogen embrittlement under elastic stress of a tempered martensitic steel. ISIJ Int. **52**, 198–207 (2012)
84. Sakaki, K., Kawase, T., Hirato, M., Mizuno, M., Araki, H., Shirai, Y., Nagumo, M.: The effect of vacancy generation in iron by plastic deformation. Scr. Mater. **55**, 1031–1034 (2006)
85. Nagumo, M., Ohta, K., Saitoh, H.: Deformation induced defects in iron revealed by thermal desorption spectroscopy of tritium. Scr. Mater. **40**, 313–319 (1999)
86. Li, S., Li, Y., Lo, Y., Neeraj, T., Srinivasan, R., Ding, X., Sun, J., Qi, L., Gumbsch, P., Li, J.: The interaction of dislocation and hydrogen-vacancy complexes and its importance for deformation-induced proto nano-voids formatin in a-Fe. Int. J. Plast. **74**, 175–191 (2015)
87. Zhu, Y., Li, Z., Huang, M., Fan, H.: Study on interactions of an edge dislocation with vacancy-H complex by atomistic modelling. Int. J. Plast. **92**, 31–44 (2017)
88. Nagumo, M., Takai, K., Okuda, N.: Nature of hydrogen trapping sites in steels induced by plastic deformation. J. Alloys Compd. **293**, 310–316 (1999)
89. Huang, Y., Nakajima, A., Nishikata, A., Tsuru, T.: Effect of mechanical deformation on permeation of hydrogen in iron. ISIJ Int. **43**, 548–554 (2003)
90. Kim, S., Kim, K.: Electrochemical hydrogen permeation measurements through high-strength steel under uniaxial tensile stress in plastic range. Scr. Mater. **66**, 1069–1072 (2012)
91. Fallahmohammadi, E., Ballinger, R., Maruno, Y., Fumagalli, G., Bolzoni, F., Re, G., Lazzari, L.: Effect of plastic deformation on hydrogen diffusion of X65 pipeline steel. In: NACE International Conference (NACE-2014-4390), San Antonio (Texas), 9–13 March 2014
92. Luu, W., Liu, P., Wu, P.: Hydrogen transport and degradation of a commercial duplex stainless steels. Corros. Sci. **44**, 1783–1791 (2002)
93. Chen, S., Wu, T., Wu, J.: Effects of deformation on hydrogen degradation in a duplex stainless steel. J. Mater. Sci. **39**, 67–71 (2004)
94. Silverstein, R., Eliezer, D., Glam, B.: Hydrogen effect on duplex stainless steels at very high strain rates. Energy Proc. **107**, 199–204 (2017)
95. Park, Y., Maroef, I., Landau, A., Olson, D.: Retained austenite as a hydrogen trap in steel welds. Welding Res. **81**, 27–35 (2002)
96. Pu, S., Turk, A., Lenka, S., Ooi, S.: Study of hydrogen release resulting from the transformation of austenite into martensite. Mater. Sci. Eng. A **754**, 628–635 (2019)
97. Claeys, L.De., Graeve, I., Depover, T., Verbeken, K.: Hydrogen-assisted cracking in 2205 duplex stainless steel: Initiation, propagation and interaction with deformation-induced martensite. Mater. Sci. Eng. A **797**, 140079 (2020)
98. Nagao, A., Dadfarnia, M., Somerday, B., Sofronis, P., O. Ritchie, R.: Hydrogen-enhanced-plasticity mediated decohesion for hydrogen-induced intergranular and "quasi-cleavage" fracture of lath martensitic steels. J. Mech. Phys. Solids **112**, 403–430 (2018)